Central Lancashire Online Knowledge (CLoK)

Title	Simulation of polarized emission from recollimation shocks in relativistic jets
Type	Article
URL	https://clok.uclan.ac.uk/id/eprint/48169/
DOI	https://doi.org/10.1093/mnras/stad2126
Date	2023
Citation	Kaye, C, Cawthorne, Timothy Vernon, Marti, J-M and Hughes, P A (2023) Simulation of polarized emission from recollimation shocks in relativistic jets. Monthly Notices of the Royal Astronomical Society, 524 (3). pp. 4765-4777. ISSN 0035-8711
Creators	Kaye, C, Cawthorne, Timothy Vernon, Marti, J-M and Hughes, P A

It is advisable to refer to the publisher's version if you intend to cite from the work.
https://doi.org/10.1093/mnras/stad2126

For information about Research at UCLan please go to http://www.uclan.ac.uk/research/

Simulation of polarized emission from recollimation shocks in relativistic jets

C. Kaye,[1] T. V. Cawthorne,[1]★ J.-M. Marti[2] and P. A. Hughes[3]

[1]*Jeremiah Horrocks Institute, University of Central Lancashire, Preston PR1 2HE, UK*
[2]*Departamento de Astronomia y Astrofisica, Universitat de Valencia, E-46100 Burjassot (Valencia), Spain*
[3]*Astronomy Department, University of Michigan, Ann Arbor, MI 48109-1107, USA*

ABSTRACT

This paper presents a method for obtaining synthetic images of linearly polarized synchrotron radiation from steady-state numerical simulations of relativistic jets, in which the magnetic field is assumed to be initially either partially or completely disordered. The method is based on the earlier work which characterized the deformation of the fluid using infinitessimal fluid elements that are initially cubic, and which evolve into parallelepipeds. The method is described for a range of models for the initial magnetic field, including ordered components that are axial, helical, and toroidal with a bi-directional axial component. The method is then applied to steady, axisymmetric simulations of initially overpressured jets and the initial results are discussed. Some characteristic patterns and trends in polarization angle are identified. Although the recollimation shocks that form in these jets are not clearly visible in the total intensity images presented here, arcs of strongly polarized emission associated with radial velocity gradients in the vicinity of the shock waves are seen, and might prove to be a useful diagnostic feature of this model.

Key words: hydrodyamics – magnetic fields – galaxies: active – galaxies: jets.

1 INTRODUCTION

The jets that emerge from active galaxies, visible as a result of the synchrotron radiation they emit, are thought to be a biproduct of the accretion of matter onto a supermassive black hole. Their speeds are relativistic, apparent superluminal motion suggesting Lorentz factors at least as high as $\simeq 20$ (e.g. Jorstad et al. 2005), and sometimes even higher (e.g. Larionov et al. 2020). At some point the jets may become overpressured relative to the ambient medium through which they flow, and this is expected to lead to an oscillation in the jet radius, as a result of the jet repeatedly overshooting its equilibrium state. This process, often referred to as recollimation, leads to the formation of internal shocks, taking the form of oppositely directed pairs of conical surfaces, coaxial with the jet (Norman & Winkler 1985). These shocks, known as recollimation shocks, have been the subject of considerable interest because their structure suggests they should possess a distinctive observational signature, particularly in polarization. This signature could be used to confirm whether or not the stationary knots seen in many astrophysical jets are caused by recollimation shocks.

Attempts to characterize the polarized emission from recollimating jets fall into two categories. First, semi-dynamical models (e.g. Cawthorne & Cobb 1990; Cawthorne 2006; Cawthorne, Jorstad & Marscher 2013; Marscher 2014) assume a simple flow model in which the changes in flow velocity are determined solely by the jump conditions at the shock. No attempt is made to follow changes in the jet velocity as fluid moves away from the shock front. The effect of the

shock on the magnetic field structure can be determined assuming the magnetic flux is frozen to the jet fluid. Secondly, relativistic magnetohydrodynamic (RMHD) simulations (Fuentes et al. 2018, 2021; Moya-Torregrosa et al. 2021) allow the flow and the magnetic field, and hence the polarized emissivity, to be calculated directly in each fluid cell. Most work using this method has assumed an ordered underlying magnetic field, for example a helical field is often used. Both methods suffer from drawbacks. The semidynamical models fail to take account of the expansion and contraction of the jet, and the assumption often made, that the emission only occurs near the shock surface, is only likely to be realistic at the highest observing frequencies. The ordered magnetic fields used in many RMHD models result in polarization fractions that are generally much higher than those observed at radio wavelengths; the weak shocks present make little impact on the field, and hence the polarization, which differs little from that expected due to the seed magnetic field, is of limited use as a diagnostic of the flow.

In considering how to continue to study the observational signatures of recollimating jets, the authors took the view that it was worth investigating a method that is capable of treating the case of a magnetic field that is disordered on scales small compared to the jet radius. The strong variations in linear polarization found in many active galaxies, particularly at optical wavelengths, are most easily explained by the presence of such a field structure (e.g. Larionov et al. 2020). Moreover, while, in any particular case, it may be possible to find an ordered field model that successfully accounts for the low polarization observed at radio frequencies, the preponderance of such low values of polarization does suggest a component of turbulent or disordered magnetic field. It is also worth noting that, while ordered field models can (with appropriately chosen parameters)

deliver polarization fractions well below the levels of $\simeq 70$ per cent expected for a uniform field (e.g. $15 - 20$ per cent in Lyutikov, Pariev & Gabuzda 2005) it is more of a challenge to get down to the levels of $5 - 10$ per cent routinely found in radio observations (e.g. Jorstad et al. 2007) in many sources. In this work, the fluid flow is determined in a full numerical simulation but a magnetic field model at injection is assumed, and then allowed to evolve as determined by magnetic flux freezing.

Due to the very substantial computing resources required to model a field that is disordered on very small scales using RMHD, an alternative approach was chosen, in which the magnetic field is assumed to be sufficiently weak to be purely passive. In this case, for any fluid element, the final magnetic field after advection can be obtained from the field at injection by simply tracking the distortion of fluid elements, and then the polarization resulting from an initially disordered magnetic field is computed by averaging the polarization over all possible directions of an intially uniform magnetic field. This approach was first used by Matthews & Scheuer (1990), and is a development of earlier methods for finding Stokes' parameters for compressed random fields by Laing (1980) and Hughes, Aller & Aller (1985); it can be applied to many types of magnetic field model, but the one for which results are presented is that in which the initial field is disordered on small scales.

At present no attempt has been made to include the effects of particle acceleration and radiative energy loss. In that sense, this work, and the earlier semidynamical work (e.g. Cawthorne 2006), represent opposite extremes of, respectively, no radiative loss and radiative loss so important that emission is only seen near the shock front. It is hoped to include radiation losses and a recipe for particle acceleration in future.

The methods that have been developed to obtain the total and polarized emission, including the emissivities for the cases of axial and helical fields with a disordered field component superimposed, are presented in Sections 3–7. The initial results from the application of this method to a numerical simulation, using the fully disordered magnetic field model, are described in Sections 8–11.

2 ASSUMPTIONS

The assumptions made in this work are as follows:

(i) A key assumption is that magnetic flux freezing applies, so that the magnetic flux threading any particular surface of a fluid element will be conserved. This assumption allows the variations in magnetic field within a fluid element to be related to changes in its shape and size.

(ii) The seed magnetic field associated with fluid injected into the numerical grid is assumed. A number of models are described in Section 4. The results presented in subsequent sections are for a field that is entirely disordered on scales small compared to grid cell. With this assumption, the field can be treated statistically, and the polarization from each cell can be averaged over all possible orientations of an initially uniform field. The other models described in Section 4 all include a component of ordered magnetic field.

(iii) Because, with available resources, we could not include the disordered magnetic field directly in RMHD simulations, it was necessary to assume that the field does not affect the simulations, i.e. that it is dynamically unimportant. This suggests using hydrodynamic simulations, though in fact, the simulations used in Sections 8–10 are RMHD simulations, but performed in the regime where the magnetic field is very weak. Different magnetic field structures were used to

check that the field geometry has no noticeable effect on the velocity field.

(iv) The deformation of fluid elements can be followed using the advection equation, which could be solved simultaneously with the Euler equations of fluid flow. The authors have attempted this approach (Kaye, Cawthorne & Hughes 2018), but were unable to implement it successfully with the computing resources available. As a result, a method based on streamlines was adopted. Here, the velocities from a single steady-state solution to the flow are used to trace streamlines, which (since the flow is steady) coincide with the pathlines of fluid elements. By tracing the pathlines joining the corners of a fluid element at injection to those further along the flow, the deformation of the fluid element can be quantified. Hence, this method requires that the flow has reached a steady state.

(v) Although the method outlined in this paper could be applied to a fully 3D simulation, the simulations used in Sections 8–10 are axisymmetric simulations. Therefore, axisymmetry is assumed. The simulation is performed in the R, z plane (z parallel to the jet axis and R the radial coordinate), and the streamlines are used to obtain the fluid deformation in this plane.

(vi) At this point, radiative losses and particle acceleration have been ignored. In the source $1803 + 784$, Cawthorne et al. (2013) found that, at 7 mm wavelength and on very long baseline interferometry (VLBI) scales, radiative losses were borderline in importance, i.e. they were just sufficiently important to justify the assumption that radiation occured predominantly near the shock front. The work presented here represents the case (at longer wavelengths, or in less luminous sources) where radiative losses make little impact on the emissivity.

(vii) The source is assumed to be optically thin. This assumption could be relaxed by adapting the formalism developed by Cawthorne & Hughes (2013).

(viii) The spectral index α (where flux density $S(\nu) \propto \nu^{-\alpha}$) is assumed to be constant, and the value $\alpha = 1$ is adopted because this makes the calculations that follow significantly easier; this is justified because (i) the chosen spectral index is close to the observed range of values ~ 0.5–1.0, and (ii) the fractional polarization has been shown to be largely unaffected by different spectral indices (Hughes et al. 1985).

3 EVALUATION OF EMISSION COEFFICIENTS

As described in Section 2, the radio emission is assumed to be optically thin. It is also assumed that the initial magnetic fields of the jet plasma are completely, or partially, disordered; a volume of plasma with a randomly tangled magnetic field would produce synchrotron emission with fractional linear polarization $\Pi \approx 0$, from any viewing angle. However, as a result of shear, compression or expansion of the jet plasma, the magnetic field (assumed to be tied to the plasma by flux freezing) may acquire a degree of order, resulting in a net linear polarization that is dependent on orientation (Laing 1980). The synchrotron emission coefficients are obtained following the methods of Matthews & Scheuer (1990), who assumed that the initial magnetic field is completely disordered; the extension of this approach to magnetic fields with ordered components is covered in Section 4. Consider a rest-frame (indicated by the primes) unit cube of plasma, initially with the uniform, flux-frozen magnetic field

$$\boldsymbol{B}'_0 = B'_{0x}\boldsymbol{a}'_0 + B'_{0y}\boldsymbol{b}'_0 + B'_{0z}\boldsymbol{c}'_0. \tag{1}$$

The z-axis is coincident with the jet axis, and the line of sight lies in the (x, z) plane. Later, this cube, with sides $\boldsymbol{a}'_0 = \hat{\boldsymbol{\imath}}$, $\boldsymbol{b}'_0 = \hat{\boldsymbol{\jmath}}$, and $\boldsymbol{c}'_0 = \hat{\boldsymbol{k}}$, becomes distorted into a parallelepiped with sides $\boldsymbol{a}'$, $\boldsymbol{b}'$, and

c', and, as shown in Matthews & Scheuer (1990), the flux-frozen magnetic field is transformed to

$$\boldsymbol{B}' = \frac{\left(B'_{0x}\boldsymbol{a}' + B'_{0y}\boldsymbol{b}' + B'_{0z}\boldsymbol{c}'\right)}{\boldsymbol{a}' \cdot \boldsymbol{b}' \times \boldsymbol{c}'}. \tag{2}$$

The spectral index is assumed to be $\alpha = 1$ (Section 2), and the relativistic electron population is assumed to have an energy distribution such that

$$dn = K\Gamma^{-2\alpha-1}d\Gamma$$

represents the (rest frame) number of particles per unit volume with Lorentz factor in the range Γ to $\Gamma + d\Gamma$. The parameter K has the value $K = K_0$ where the particles are first injected. Subsequently, the value of K varies with the rest-frame volume of the parallelepiped, $V' = |\boldsymbol{a}'.(\boldsymbol{b}' \times \boldsymbol{c}')|$ according to

$$K = K_0 V'^{(-1-2\alpha/3)}$$

due to adiabatic expansion or compression. The Stokes parameters for synchrotron radiation from such a fluid element can be found in terms of the components of the vectors $\boldsymbol{a}'$, $\boldsymbol{b}'$, $\boldsymbol{c}'$, resolved into components parallel to the l, m, and n axes, where n is directed toward the observer, l lies in the plane of n and the particle velocity, $\boldsymbol{v}$, perpendicular to n, and m is perpendicular to both l and n such that the l, m, and n axes form a right handed system. With these definitions, it follows from Matthews & Scheuer (1990; their equations 2.6 and 2.8) that the emission coefficients, expressed in the rest frame of the fluid element, are

$$\langle j'_I \rangle = \frac{CK}{V'^2}\Bigg(\langle B'^2_{0x}\rangle (a'^2_l + a'^2_m) + \langle B'^2_{0y}\rangle (b'^2_l + b'^2_m) $$
$$+ \langle B'^2_{0z}\rangle (c'^2_l + c'^2_m) + 2\langle B'_{0x}B'_{0y}\rangle(a'_l b'_l + a'_m b'_m) $$
$$+ 2\langle B'_{0x}B'_{0z}\rangle(a'_l c'_l + a'_m c'_m) + 2\langle B'_{0y}B'_{0z}\rangle(b'_l c'_l + b'_m c'_m) \Bigg), \tag{3a}$$

$$\langle j'_Q \rangle = \frac{3CK}{4V'^2}\Bigg(\langle B'^2_{0x}\rangle \left(a'^2_l - a'^2_m\right) + \langle B'^2_{0y}\rangle \left(b'^2_l - b'^2_m\right) $$
$$+ \langle B'^2_{0z}\rangle \left(c'^2_l - c'^2_m\right) + 2\langle B'_{0x}B'_{0y}\rangle(a'_l b'_l - a'_m b'_m) $$
$$+ 2\langle B'_{0x}B'_{0z}\rangle(a'_l c'_l - a'_m c'_m) + 2\langle B'_{0y}B'_{0z}\rangle(b'_l c'_l - b'_m c'_m) \Bigg), \tag{3b}$$

$$\langle j'_U \rangle = \frac{3CK}{2V'^2}\Bigg(\langle B'^2_{0x}\rangle a'_l a'_m + \langle B'^2_{0y}\rangle b'_l b'_m + \langle B'^2_{0z}\rangle c'_l c'_m $$
$$+ \langle B'_{0x}B'_{0y}\rangle(a'_l b'_m + b'_l a'_m) + \langle B'_{0x}B'_{0z}\rangle(a'_l c'_m + c'_l a'_m) $$
$$+ \langle B'_{0y}B'_{0z}\rangle(b'_l c'_m + c'_l b'_m) \Bigg). \tag{3c}$$

The terms inside the angle brackets represent the values of the coefficients for a particular orientation of the initial magnetic field, $\boldsymbol{B_0}$. Account is taken of the disordered nature of the initial field by averaging over all such orientations, as indicated by the angle brackets. The constant C depends on fundamental constants, and can be obtained from any text on synchrotron theory.

4 MAGNETIC FIELD MODELS

In this section, the Stokes parameters emissivities are obtained for four particular field models, including both wholly and partially disordered fields.

4.1 Purely disordered field

An initially uniform magnetic field is given in terms of conventional polar coordinates θ and ϕ, by

$$\boldsymbol{B}'_0 = B_r \left(\sin\theta \left(\cos\phi \hat{\boldsymbol{\imath}} + \sin\phi \hat{\boldsymbol{\jmath}}\right) + \cos\theta \hat{\boldsymbol{k}}\right),$$

where B_r is the (rest frame) flux density of the randomly tangled component of magnetic field; when the squared terms are averaged over all initial orientations (θ, ϕ) of the field,

$$\left\langle B'^2_{0x}\right\rangle = \left\langle B'^2_{0y}\right\rangle = \left\langle B'^2_{0z}\right\rangle = \frac{B_r^2}{3},$$
$$\langle B'_{0x}B'_{0y}\rangle = \langle B'_{0x}B'_{0z}\rangle = \langle B'_{0y}B'_{0z}\rangle = 0,$$

and therefore, from equation (3), the corresponding Stokes parameter emissivities in the rest frame of the fluid element are

$$\langle j'_I \rangle = \frac{CKB_r^2}{3V'^2}\left(a'^2_l + b'^2_l + c'^2_l + a'^2_m + b'^2_m + c'^2_m\right), \tag{4a}$$

$$\langle j'_Q \rangle = \frac{CKB_r^2}{4V'^2}\left(a'^2_l + b'^2_l + c'^2_l - a'^2_m - b'^2_m - c'^2_m\right), \tag{4b}$$

$$\langle j'_U \rangle = \frac{CKB_r^2}{2V'^2}\left(a'_l a'_m + b'_l b'_m + c'_l c'_m\right). \tag{4c}$$

as found earlier by Matthews & Scheuer (1990).

4.2 Disordered field with an axial component

For an initially randomly tangled magnetic field that also has a component parallel to the jet-axis of magnitude $B_\parallel$, the field is given by

$$\boldsymbol{B}'_0 = B_r \sin\theta \left(\cos\phi \hat{\boldsymbol{\imath}} + \sin\phi \hat{\boldsymbol{\jmath}}\right) + \left(B_r \cos\theta + B_\parallel\right)\hat{\boldsymbol{k}}.$$

Upon spatially averaging the squared components,

$$\left\langle B'^2_{0x}\right\rangle = \left\langle B'^2_{0y}\right\rangle = \frac{B_r^2}{3},$$
$$\left\langle B'^2_{0z}\right\rangle = \frac{B_r^2}{3} + B_\parallel^2,$$
$$\langle B'_{0x}B'_{0y}\rangle = \langle B'_{0x}B'_{0z}\rangle = \langle B'_{0y}B'_{0z}\rangle = 0,$$

and so the Stokes parameters according to equation (3) are

$$2\langle j'_I \rangle = \frac{CK}{V'^2}\Bigg(\frac{B_r^2}{3}\left(a'^2_l + b'^2_l + c'^2_l + a'^2_m + b'^2_m + c'^2_m\right) $$
$$+ B_\parallel^2\left(c'^2_l + c'^2_m\right) \Bigg), \tag{5a}$$

$$\langle j'_Q \rangle = \frac{3CK}{4V'^2}\Bigg(\frac{B_r^2}{3}\left(a'^2_l + b'^2_l + c'^2_l - a'^2_m - b'^2_m - c'^2_m\right) $$
$$+ B_\parallel^2\left(c'^2_l - c'^2_m\right) \Bigg), \tag{5b}$$

$$\langle j'_U \rangle = \frac{3CK}{2V'^2}\left(\frac{B_r^2}{3}\left(a'_l a'_m + b'_l b'_m + c'_l c'_m\right) + B_\parallel^2 c'_l c'_m\right). \tag{5c}$$

4.3 Disordered field with a helical component

It has been argued that jets may contain a helical component of magnetic field, possibly a relic of the extraction of plasma from a spinning accretion disc (e.g. Murphy, Cawthorne & Gabuzda 2013). For a magnetic field that is randomly tangled, but also has a component B_h that is helically ordered with a pitch angle φ to the

jet-parallel axis, the corresponding magnetic field is

$$
\begin{aligned}
\boldsymbol{B}'_0 = {} & (B_r \sin\theta \cos\phi - B_h \sin\varphi \sin\psi)\hat{\boldsymbol{\imath}} \\
& + (B_r \sin\theta \sin\phi + B_h \sin\varphi \cos\psi)\,\hat{\boldsymbol{\jmath}} \\
& + (B_r \cos\theta + B_h \cos\varphi)\hat{\boldsymbol{k}},
\end{aligned}
$$

where ψ is the the position angle of the fluid element in the plane normal to the jet axis, measured from the x-axis towards the y-axis. Spatially averaging the squared magnetic field components for this field, we find

$$
\left\langle B_{0x}'^{\,2} \right\rangle = \frac{B_r^2}{3} + B_h^2 \sin^2\varphi \sin^2\psi, \quad \left\langle B_{0x}' B_{0y}' \right\rangle = -\frac{B_h^2}{2} \sin^2\varphi \sin(2\psi),
$$

$$
\left\langle B_{0y}'^{\,2} \right\rangle = \frac{B_r^2}{3} + B_h^2 \sin^2\varphi \cos^2\psi, \quad \left\langle B_{0x}' B_{0z}' \right\rangle = -\frac{B_h^2}{2} \sin(2\varphi) \sin\psi,
$$

$$
\left\langle B_{0z}'^{\,2} \right\rangle = \frac{B_r^2}{3} + B_h^2 \cos^2\varphi, \quad \left\langle B_{0y}' B_{0z}' \right\rangle = \frac{B_h^2}{2} \sin(2\varphi) \cos\psi.
$$

The resulting expressions for $\left\langle j_I' \right\rangle$, $\left\langle j_Q' \right\rangle$, and $\left\langle j_U' \right\rangle$ are easily found from equation (3), but are rather lengthy and so are not reproduced here.

4.4 Toroidal field, bi-directional axial field, and a disordered field component

In this model the axial field component is uniform in magnitude, but can be either parallel or antiparallel to the z-axis, with equal probability. This model has similarities to the helical field model, but carries zero net magnetic flux. Such a model would be appropriate if, for example, the axial field consists of loops that have been stretched in the z direction. The magnetic field is given by

$$
\begin{aligned}
\boldsymbol{B}'_0 = {} & (B_r \sin\theta \cos\phi - B_t \sin\psi)\hat{\boldsymbol{\imath}} \\
& + (B_r \sin\theta \sin\phi + B_t \cos\psi)\,\hat{\boldsymbol{\jmath}} \\
& + (B_r \cos\theta + f B_a)\hat{\boldsymbol{k}},
\end{aligned}
$$

where B_r, B_t, and B_a are the constant magnitudes of the random, toroidal, and axial field components, respectively, and the parameter f, which controls the direction of the axial field, takes the values $+1$ and -1 with equal probability. Averaging over θ, ϕ, and f, it is easily seen that

$$
\left\langle B_{0x}'^{\,2} \right\rangle = \frac{B_r^2}{3} + B_t^2 \sin^2\psi, \quad \left\langle B_{0x}' B_{0y}' \right\rangle = -\frac{B_t^2}{2} \sin(2\psi),
$$

$$
\left\langle B_{0y}'^{\,2} \right\rangle = \frac{B_r^2}{3} + B_t^2 \cos^2\psi, \quad \left\langle B_{0x}' B_{0z}' \right\rangle = 0,
$$

$$
\left\langle B_{0z}'^{\,2} \right\rangle = \frac{B_r^2}{3} + B_a^2, \quad \left\langle B_{0y}' B_{0z}' \right\rangle = 0.
$$

The averaged emission coefficients are then found by substitution into equation (3), as in the previous examples.

5 STREAMLINE-BASED PARALLELEPIPED MONITORING

This section describes a method of following the deformation of the plasma using streamlines of a steady flow. In a steady flow, pathlines and streamlines are one and the same, so that the trajectory of any point embedded in the flow can be obtained from the velocity field at a single point in time. The method is similar to that used by Matthews & Scheuer (1990), who injected marker particles into the base of the flow at regular intervals, and followed their pathlines through the simulation. By monitoring the positions of the particles at the vertices of an infinitesimal (or in practice, small) and initially
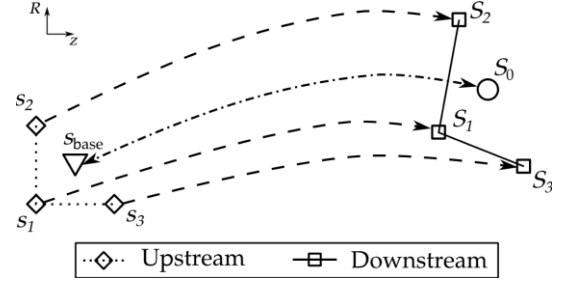
Figure 1. Schematic showing the marker particles advected, and how the change in particle separation gives the evolved parallelepiped vectors.T

cubic volume, the evolution of the cube into a parallelepiped may be followed, and the parallelepiped vectors found from the changes in vertex separation. An unfortunate result of this method is that the distribution of marker particles depends on the evolution of the flow, and becomes very irregular far from the injection plane. This leads to the difficult problem of interpolating the parallelepiped vectors from an irregularly sampled grid.

To avoid the problem of an irregular distribution of parallelepipeds, a set of parallelepiped vectors is obtained for every grid point. This is done by advecting particles centred on each grid point, s_0, backwards for N iterations, to a point s_{base}, no more than one pixel from the inlet plane. A marker particle is then advected forwards from s_{base} for N time steps, in order to verify the accuracy of the calculated streamline. If the final position of the marker particle is equal to s_0 with a tolerance of 1 per cent of the grid resolution then the streamline is accepted. (With the simulations used in Sections 8–11, the mean discrepancy was of order $\sim 10^{-4}$ per cent of the grid spacing.) Although this method is applicable to 3D simulations, the discussion here assumes 2D axisymmetry as appropriate to the simulations used in Sections 8–11. The distortion in the $R-z$ plane of a 2D axisymmetric simulation can be followed by releasing three further marker particles at the vertices of a square enclosing s_{base}. An illustration of the marker-particles advection is shown in Fig. 1. Then,

$$
s_1 = s_{\text{base}} - \frac{\delta_{xyz}}{2C}\left(\hat{\boldsymbol{R}} + \hat{\boldsymbol{k}}\right)
$$

$$
s_2 = s_{\text{base}} + \frac{\delta_{xyz}}{2C}\left(\hat{\boldsymbol{R}} - \hat{\boldsymbol{k}}\right), \text{ and}
$$

$$
s_3 = s_{\text{base}} + \frac{\delta_{xyz}}{2C}\left(-\hat{\boldsymbol{R}} + \hat{\boldsymbol{k}}\right) \tag{6}
$$

where δ_{xyz} is the grid coordinate separation and C is a constant that determines the initial size of the particle; $C = 2$ was chosen for the work presented here. Advecting forward from these positions for N time steps, the three marker particles are displaced to positions S_1, S_2, and S_3, from which the deformed parallelepiped vectors in the R, z plane can be found. The parallelepiped unit vectors initially parallel to the R and z axes become, respectively, $\Delta\boldsymbol{R} = C(S_2 - S_1)$ and $\Delta\boldsymbol{z} = C(S_3 - S_1)$ (the factors of C scaling for a vector initially of unit length).

In axisymmetry, the parallelepiped vector initially in the azimuthal direction, $\Delta\boldsymbol{\phi}$, is stretched in proportion to the change in radial coordinate. If the radial coordinates of s_0 and s_{base} are, respectively, R_0 and R_{base}, then $\Delta\boldsymbol{\phi} = (R_{\text{base}}/R_0)\hat{\boldsymbol{\phi}}$.

To advect a particle from its position $s(i)$ at the ith time step by one iteration, an initial estimate of $s(i + 1)$ is provided by

$$
s(i + 1) = s(i) + v(i)\delta t, \tag{7}
$$

where the velocity is $v(i) = v(s(i))$. The off-grid velocities are determined via bilinear interpolation. The average velocity during this time step is

$$\bar{v} = \frac{1}{2}\left(v(i) + v(i+1)\right), \tag{8}$$

and so our revised estimate of the destination of the particle at the end of the time step is then

$$s(i+1) = s(i) + \bar{v}\delta t. \tag{9}$$

Note that

$$s(i+1) = s(i) + v(i)\delta t + \frac{1}{2}\left(\frac{v(i+1) - v(i)}{\delta t}\right)\delta t^2,$$
$$= s(i) + v(i)\delta t + \frac{1}{2}\bar{a}(i)\delta t^2, \tag{10}$$

where $\bar{a}(i)$ is the average acceleration between the ith and the $(i+1)$th time steps. This shows that the increments in δt are equivalent to assuming uniform acceleration over the time step.

6 OBTAINING EXTRAPLANAR PARALLELEPIPEDS

For radiative transfer it is preferable to have the parallelepiped vectors on a Cartesian grid. In this section the vectors $\Delta \boldsymbol{R}$, $\Delta \boldsymbol{z}$, and $\Delta \boldsymbol{\phi}$ are transformed, using axisymmetry, into a set of parallelepiped vectors $\boldsymbol{a}$, $\boldsymbol{b}$, and $\boldsymbol{c}$, initally parallel to $\boldsymbol{i}$, $\boldsymbol{j}$, and $\boldsymbol{k}$, respectively.

Consider a displacement vector $\boldsymbol{g}$ with ends embedded in the flow. It has cylindrical polar coordinates (g_R, g_ϕ, g_z) that evolved from their initial values $(g_{R0}, g_{\phi0}, g_{z0})$. Then, the initial and final coordinates are related by

$$\begin{pmatrix} g_R \\ g_\phi \\ g_z \end{pmatrix} = \begin{pmatrix} \Delta R_R & 0 & \Delta z_R \\ 0 & \Delta \phi_\varphi & 0 \\ \Delta R_z & 0 & \Delta z_z \end{pmatrix} \begin{pmatrix} g_{R0} \\ g_{\phi0} \\ g_{z0} \end{pmatrix}. \tag{11}$$

At azimuthal coordinate, ϕ, the transformations between the Cartesian and cylindrical coordinate systems are given by

$$\begin{pmatrix} g_R \\ g_\phi \\ g_z \end{pmatrix} = \begin{pmatrix} \cos\phi & \sin\phi & 0 \\ -\sin\phi & \cos\phi & 0 \\ 0 & 0 & 1 \end{pmatrix} \begin{pmatrix} g_x \\ g_y \\ g_z \end{pmatrix}, \tag{12a}$$

$$\begin{pmatrix} g_x \\ g_y \\ g_z \end{pmatrix} = \begin{pmatrix} \cos\phi & -\sin\phi & 0 \\ \sin\phi & \cos\phi & 0 \\ 0 & 0 & 1 \end{pmatrix} \begin{pmatrix} g_R \\ g_\phi \\ g_z \end{pmatrix}. \tag{12b}$$

Then, for example, the value of the parallelepiped vector $\boldsymbol{a}$, initially $(1, 0, 0)$ in Cartesian coordinates, or $(\cos\phi, -\sin\phi, 0)$ in cylindrical coordinates (from equation 12a), is deformed by the flow into $(\Delta R_R \cos\phi, -\Delta\phi_\varphi\sin\phi, \Delta R_z\cos\phi)$, according to equation (11). Transforming back into Cartesian coordinates using equation (12b), we obtain the value of $\boldsymbol{a}$, evolved by the flow, to be

$$\boldsymbol{a} = \left(\Delta R_R \cos^2\phi + \Delta R_\varphi \sin^2\phi, \left(\Delta R_R - \Delta\phi_\varphi\right)\sin\phi\cos\phi, \Delta R_z\cos\phi\right). \tag{13}$$

Similarly for $\boldsymbol{b}$ and $\boldsymbol{c}$ in Cartesian coordinates:

$$\boldsymbol{b} = \left(\left(\Delta R_R - \Delta\phi_\varphi\right)\sin\phi\cos\phi, \Delta R_R\sin^2\phi + \Delta\phi_\varphi\cos^2\phi\Delta, R_z\sin\phi\right) \tag{14}$$

$$\boldsymbol{c} = \left(\Gamma_{\text{base}}^{-1}\Delta z_R\cos\phi, \Gamma_{\text{base}}^{-1}\Delta z_R\sin\phi, \Gamma_{\text{base}}^{-1}\Delta z_z\right), \tag{15}$$

where Γ_{base} is the *flow* Lorentz factor at the base of the jet. The appearance of Γ_{base} in equation (15) is explained at the end of this Section.

In summary, therefore, the streamline analysis of Section 5 can be applied to the velocity output from a steady-state simulation to provide a set of parallelepiped vectors describing the deformation of the plasma as a result of its passage through the jet. The results given above correspond to a 2D axisymmetric simulation, with parallelepiped vectors calculated in the R, z, ϕ system, which can then be rotated (using equations 13–15) into the Cartesian system to give $\boldsymbol{a}$, $\boldsymbol{b}$, and $\boldsymbol{c}$, the corresponding vectors initally parallel to the x-, y-, and z-axis, respectively.

The parallelepiped vectors are determined in the (laboratory) frame of the simulation. To find the emission coefficients, their values $\boldsymbol{a}'$, $\boldsymbol{b}'$, and $\boldsymbol{c}'$ in the fluid rest frame are required, and it is these that are required to be, initially, a set of orthogonal unit vectors. Since the flow is initially parallel to the z-axis with Lorentz factor Γ_{base}, $\boldsymbol{a}_0 = \boldsymbol{a}'_0$, $\boldsymbol{b}_0 = \boldsymbol{b}'_0$ and $\boldsymbol{c}_0 = \boldsymbol{c}'_0/\Gamma_{base}$. To ensure that $\boldsymbol{c}'$ is initially a unit vector, value of $\boldsymbol{c_0}$ is reduced by a factor of Γ_{base}, the Lorentz factor at the base.

7 TRANSFORMATION OF EMISSIVITIES AND RADIATION TRANSFER

The parallelepiped vectors $\boldsymbol{a}$, $\boldsymbol{b}$, and $\boldsymbol{c}$ are easily transformed into the fluid rest frame at each point by resolving into components parallel and perpendicular to the fluid velocity. They can then be rotated into the l, m, n frame, as defined in Section 3, to provide the components a'_l, a'_m, and a'_n (and similarly for b and c) required to obtain the emissivities. These are then transformed into the laboratory frame using $j = j' D^{2+\alpha}$ (e.g. Rybicki & Lightman 1979) (where D is the Doppler factor). The polarization angle, referred to the l and m axes, is Lorentz invariant (i.e $\chi_{l,m} = \chi'_{l,m}$) with respect to the corresponding axes defined in the observer frame, and so can be found directly from $\tan(2\chi_{l,m}) = j'_U/j'_Q$, but since the l and m axis vary in orientation over the grid (due to changes in fluid velocity) the polarization angle must now be referred to a fixed set of axes in the sky plane, such as the y-axis and the vector $\hat{\boldsymbol{j}} \times \hat{\boldsymbol{n}}$ (where $\hat{\boldsymbol{j}}$ is the unit vector parallel to the y-axis). The Stokes emissivities for each grid point can then be referred to this fixed pair of axes, and finally integrated along the line of sight to give the the I, Q, and U intensities for each pixel in the sky plane.

8 APPLICATION TO NUMERICAL SIMULATIONS

Here, the methods presented in the preceding sections are applied to a set of steady-state numerical simulations. The simulations used here employ a 'quasi-one-dimensional', axisymmetric, time-independent code described by Fuentes et al. (2018, FGMP from now on), following the approach of Komissarov, Porth & Lyutikov (2015). The resulting simulations, represent initially overpressured jets in which recollimation shocks occur (Norman & Winkler 1985). In the method presented earlier, the velocity field of the simulation is used to follow the distortion of the fluid elements as they pass through the jet. The distortion is characterized by vectors that span small fluid elements that are initially cubic, and evolve into parallelepipeds as they progress through the jet, due to expansion, compression, and shear. The magnetic field associated with the injected plasma is assumed to be disordered on scales much smaller than the jet radius at the injection plane, but acquires a degree of order due to the plasma distortion. As a result, any synchrotron emission from relativistic electrons in the jet will be linearly polarized to some extent. The Stokes parameters from each fluid element can be determined, and integrated along lines of sight to obtain simulated images of total

Table 1. Parameters of MHD jet models in the inlet plane.

Simulation	ϵ (c^2)	v/c	p_{tot}^*	$\mathcal{B}$ (per cent)	B_ϕ/B_z
Hot	10.3	0.950	2.05	1.51	28.7
Warm	1.2	0.950	2.29	9.39	4.6
Cold	0.3	0.950	2.05	1.51	45.5

Note. Tabulated data denote the jet model, specific internal energy, velocity, and total pressure at the centre of the jet inlet plane, and the maximum ratio of magnetic-to-gas pressure, the ratio of peak azimuthal and axial magnetic field components, and the radius of the jet at the inlet plane, in that order. Values are given to a maximum of three significant figures, and the symbol * denotes that the term is a ratio between the value on the jet axis at the inlet, and in the ambient medium.

and linearly polarized intensity, and electric vector position angle (EVPA). The fluid simulation code of Fuentes et al. (2018) requires the plasma to possess an ordered magnetic field (the field used was helical) but the three simulations chosen are all 'weak field' cases, in which the ratio of magnetic pressure to gas pressure, $\mathcal{B}$ is everywhere less than 10 per cent, and the mean ratio of magnetic-to-gas pressure is 1 per cent in all three cases. In these circumstances, the field structure has a negligible effect upon the kinematics of the flow.

The three models presented here are summarized in Table 1. The inlet plane velocity is 0.95c in all cases, and directed parallel to the jet axis. The models are characterized by the rest frame ratios of internal energy density to rest mass energy density at injection, ϵ, given in the first column, and are referred to as 'hot', 'warm', and 'cold', according to the value of ϵ. In addition, three other models with the same ϵ as the hot model, but with different initial magnetic field structures, were examined. The four models with this value of ϵ were found to possess nearly identical velocity distributions. This provides a justification for replacing the initial magnetic field by a different model (in this paper, a disordered field) and assuming that the evolution of the fluid flow will be unaffected.

Each of the simulations has the same resolution in the r–z plane, extending 160 pixels in the radial direction, and 8000 pixels along the jet axis. The Lorentz factor profiles of the first three recollimation shocks (RSs) in the jets of hot, warm and cold simulations can be seen in Fig. 2, each panel with independent aspect ratios and colour-bars. The typical cone shaped RSs are clearly highlighted by the areas of high velocity gradient. The plots show that they are closer together and have greater obliquity in the hotter jet models, which is expected since the shock spacing is proportional to the Mach number of the flow (e.g. Falle & Wilson 1985); the Mach numbers are lower for the hotter simulations. The hotter models also display a greater range of Lorentz factors within the flow. This is as expected since the hotter jets have greater internal energy available for conversion into kinetic energy. The fluid of the kinetically dominated cold simulation is able to reach approximately the same speed upon arriving at each RS front due to the relatively weak nature of these shocks; the hotter jets, however, have stronger RSs and achieve significantly lower Lorentz factors upon reaching each successive RS. As noted by Fuentes et al. (2018), the multiple RSs seen within a single simulation appear similar, but because crossing a shock is an irreversible process, and entropy is not conserved, the shocks do differ from one to the next. After the first RS, the structure of each shock is also more complex, consisting of a principal conical shock together with one or more secondary overlapping conical shocks; these secondary shocks are a result of reflections from the simulation jet boundary.

In each case, the Lorentz factor profile is uniform across the inlet plane, falling rapidly to unity (for stationary fluid) outside a radius

of 61.5 grid cells from the axis. Streamlines for this radius were projected forward and used to define the envelope of the jet. It is assumed that only fluid within this envelope emits synchrotron radiation.

Using the velocities output from the simulations, emissivities were calculated, and Stokes' parameters were thereby obtained (assuming optically thin emission) as described in the previous sections. The results are presented below.

9 VARIATION OF POLARIZATION WITH JET INCLINATION

This section presents a description of the variation of polarization in the simulated jets with angle between the jet axis and the line of sight. The simulated jet structures can be described as a series of bubbles and pinch points. A pinch point refers to a point on axis at which the jet radius is a local minimum. A bubble centre refers to a point on axis at which the jet radius is a local maximum. To facilitate this study, the polarization and total intensity have been determined at the centres of the first bubble and first pinch point, as seen in the simulated images, for a range of angle, θ (between line of sight and the jet axis), between 5° and 30°. Lines of sight that pass through the centres of the bubbles and pinch points lie entirely in the symmetry plane containing the jet axis and the line of sight, and therefore have Stokes $U = 0$, and EVPA either parallel (for $Q > 0$) or perpendicular ($Q < 0$) to the projected jet axis.

The results for the first bubble are shown in Figs 3 (showing Stokes Q) and 4 (showing fractional polarization, i.e. $|Q|/I$). Results are shown for angles greater than 5° because, for smaller angles, the results are complicated by the passage of the line of sight through the off-axis parts of at least two of the RS.

The variation of polarization with θ is similar for all three simulations. At smaller angles, Q is negative, but as θ increases, Q becomes positive, and the polarization electric vectors flip through 90°, from perpendicular to parallel to the jet axis.

The positive Q values seen at large θ are as expected for stretching of the disordered magnetic field in the plane perpendicular to the jet axis, as the gas passes into the bubble. The fractional polarization is generally larger for the colder bubble and least for the hot bubble. The main reason for this is that the Lorentz factor of the flow increases within the bubble and increases most for the hot simulation (Fig. 2). As a result, for a viewing angle of 20°, the rest frame viewing angle at this location is about 130° for the hot simulation, but close to 100° for the cold simulation. The cold simulation is therefore viewed (in the fluid rest frame) from a direction closer to plane normal to the jet axis, where the fractional polarization is greatest. The greater expansion in the hot bubble also means the field has been more highly ordered.

The reason for the negative Q values at small θ turns out to be that, for such small angles, the line of sight intersects thin, annular regions at the surface of the jet, near its base, where the jet just started to expand sideways. Here the plasma has been stretched radially, giving a magnetic field that becomes quite highly ordered, and has an average direction with sky-projection parallel to the jet so that the resulting EVPAs indicate a direction perpendicular to the projected axis.

The change to negative Q occurs for smaller angles in the colder simulations because the bubbles are longer in these, and so the line of sight intersects these regions of more highly ordered field at smaller angles in the colder than in the hotter jets. Figs 5 and 6 show, respectively, Stokes Q and fractional polarization for lines of sight through the centre of the first pinch point, as a function of θ. In the simulations presented here this is the brightest part of the jet,
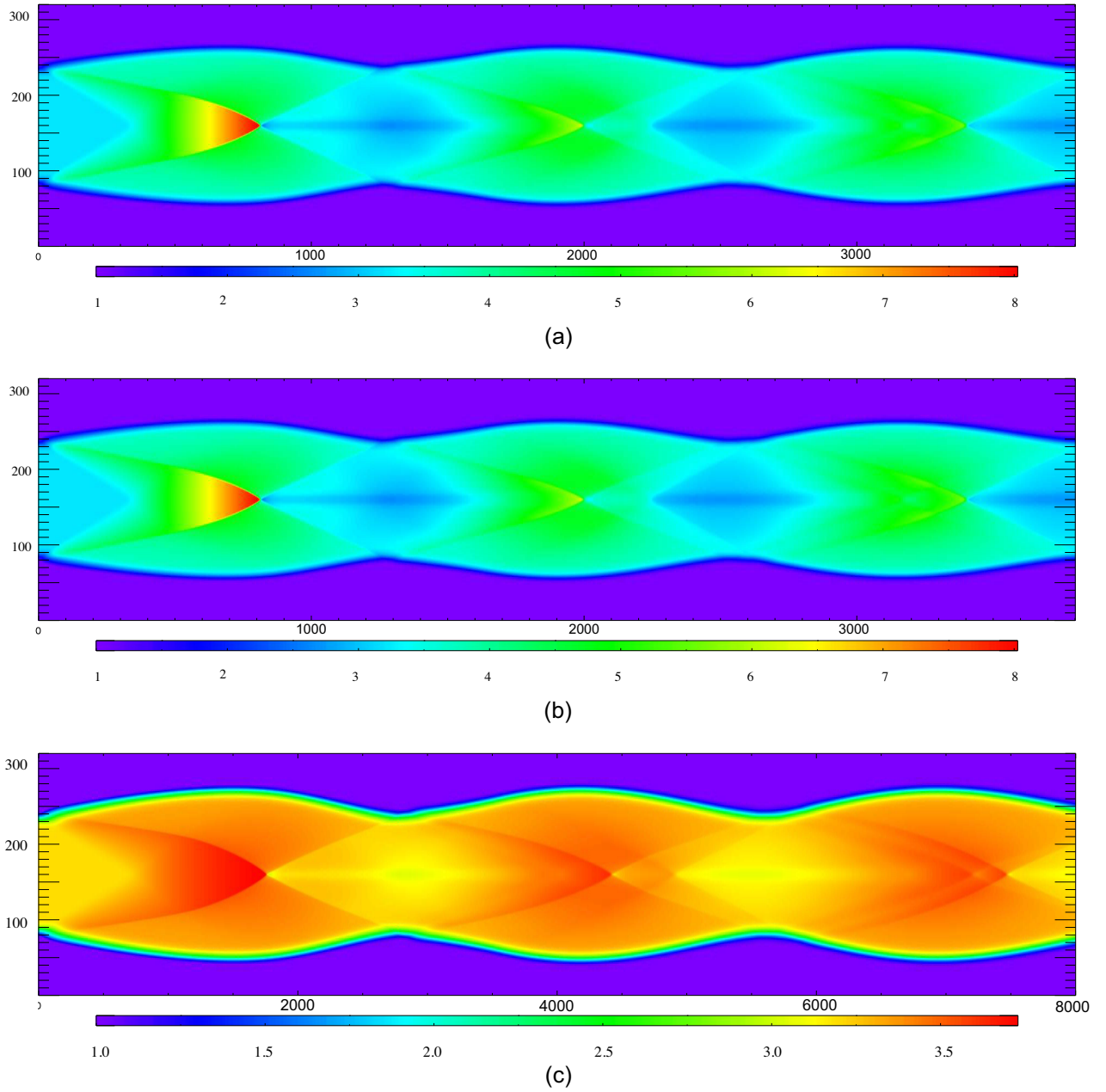
Figure 2. Lorentz factor profiles of a hot, intermediate, and cold jet, from top-to-bottom, respectively. Note the different scales along the jet axis, and on the colour bar, in the three cases. In the hotter simulations there is a larger range of Lorentz factor, and the shocks are more closely spaced.
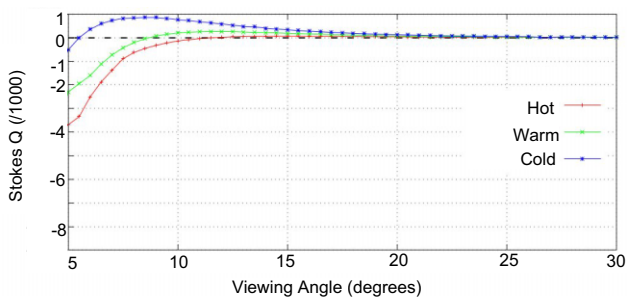

Figure 3. Graph showing the variation of Stokes Q (in arbitrary units) at the first bubble centre with angle θ between the axis and line of sight.
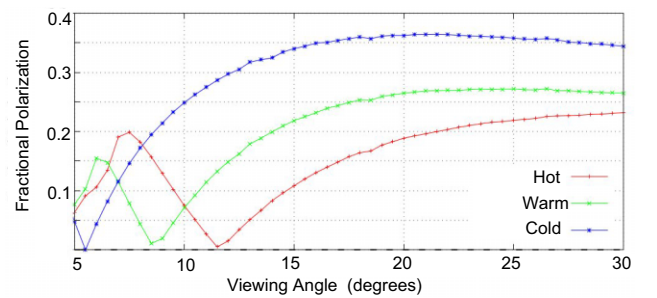
Figure 4. Graph showing the variation of fractional polarization at the first bubble centre with angle θ between the axis and line of sight.
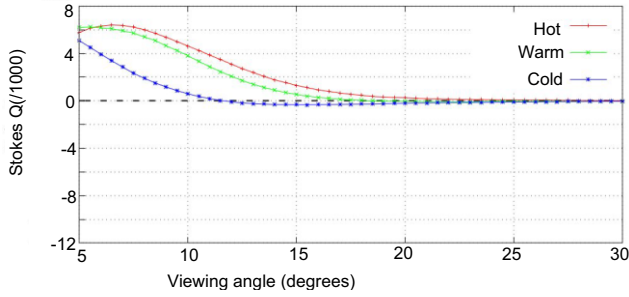
Figure 5. Graph showing the variation of Stokes Q (in arbitrary units) at the first centre of the first pinch point with angle θ between the axis and line of sight.
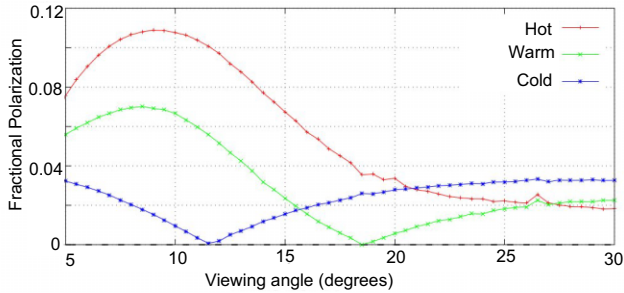
Figure 6. Graph showing the variation of fractional polarization at the centre of the first pinch point with angle θ between the axis and line of sight.

due to the enhancement of emissivity that accompanies compression, but the fractional polarization is generally much lower than in the bubble. This is a result of the jet's return to a radius close to its value at injection, and hence a magnetic field structure that possesses a very low degree of order. The fact that the polarization is not quite zero is a result of (i) the unequal spacing of the stream lines at the pinch point and (ii) the fact that this near-initialized state exists only at one value of z, and the line of sight intersects a large range of z values.

The figures show that at smaller θ values, $Q > 0$, so electric vectors are parallel to the projected jet axis. In the cold and intermediate simulations only, the polarization vectors flip through 90° at larger angles. In this case, the variations in Q with θ are not generally amenable to simple explanations, resulting as they do from the passage of the line of sight through multiple regions with different field structures, the relative contributions of which change as the line of sight changes.

Overall, the bubbles and pinch points show very different polarization behaviour. For lines of sight through the bubble's centre, the electric vectors are parallel to the projected jet axis at larger line-of-sight angles, θ, becoming perpendicular at smaller θ; the colder models are generally more highly polarized. For lines of sight through the pinch point, electric vectors are perpendicular to the jet axis at larger θ, becoming parallel at smaller θ; the hotter models are generally more highly polarized.

10 SIMULATED IMAGES

The previous section discussed trends in polarization at the widest and narrowest parts of the simulated jet as the line-of-sight angle θ varies. In this section, images showing the spatial variation of total intensity and fractional polarization are shown for certain discrete values of θ, namely, $\theta = 5^\circ$, 10°, and 20° for the hot (Fig. 7),

warm (Fig. 8), and cold (Fig. 9) simulation. In these plots, total intensity, I, in arbitrary units, is represented by a colour scale, and polarization is represented by lines of length proportional to linearly polarized intensity, P, and orientation parallel to the electric field of the wave. Note that the scaling of intensity has been performed independently for each of the images. The corresponding colour plots showing fractional polarization are shown in Figs 10, 11, and 12 for, respectively, the hot, warm, and cold cases. Values of fractional polarization are shown by the colour bars.

The brightest parts of the jet are the pinch points. The adiabatic relationship between pressure and density ensures that where the jet is most dense, the total intensity is highest. In these simulations, this effect dominates a reduction in the levels of relativistic boosting at the pinch points, due to the Lorentz factor being minimal at these positions. However, the balance between compression and relativistic boosting may well be different for simulations with differing parameters, particularly the initial Lorentz factor. The polarized intensity is also the highest at these points.

The trends noted in the previous section are apparent, most clearly in the 'warm' simulation case (Fig. 8), where the 90 degree change in polarization angle between the smallest and largest line-of-sight angles shown, can be clearly seen, both at the centre of the bubble and the pinch point. The low fractional polarization around the pinch points is also apparent.

In most cases, the conical shock waves, which radiate outward from a point on the axis slightly forward of the centre of the bubble, make only a minor impact on the total or polarized intensity. The outline of the reflected (diverging) shock can be seen as a faint enhancement in the warm jet simulation at $\theta = 20^\circ$ in total intensity (Fig. 8) and in the corresponding image for polarized intensity (Fig. 13).

Due to their relative weakness, the effect of the compression that occurs at the shock front is small compared to the effects due to the expansion and contraction of the jet. However, in this work, the effect of particle acceleration near shock fronts has not been included, and, if this process contributes significantly to the population of radiating electrons, then the effect of the shock fronts may be much more pronouced than suggested by these results. Note that, although particle acceleration at the shock fronts is very likely to occur, theory suggests that most of the energy goes into ions (if such are present), and the amount that reaches the electron population is open to conjecture (Warren et al. 2015).

Although the shock itself is not visible in most of the plots shown here, prominent arcs of high fractional polarization are seen near to the shock positions. These arcs spread outward from positions roughly coincident with the apexes of the conical shock wave. To make this clearer, Fig. 14 shows an outline of the radial extent of the shock wave, superimposed on a plot of fractional polarization, for the hot model. The position of the shock wave was determined by making a plot of the gradient of Γv_z along the z-axis (where Γ is the Lorentz factor) – by far the largest values occur at the location of the shock. The figure shows that the arcs of high polarization lie near the outer boundary of the shock wave.

The formation of these regions of high fractional polarization can be understood from the radial velocity distribution. Where the incident (or converging) shock waves meet the surface of the the jet, a strong radial velocity gradient *inside* the shock can be seen, with v_r increasing rapidly with r. The plasma in this region is therefore being stretched radially, strongly ordering the magnetic field field in the outer part of the jet. A similar effect is seen *outside* the (reflected) diverging shock wave, where in the region before the shock, v_r is negative, and $|v_r|$ decreases strongly as r increases.
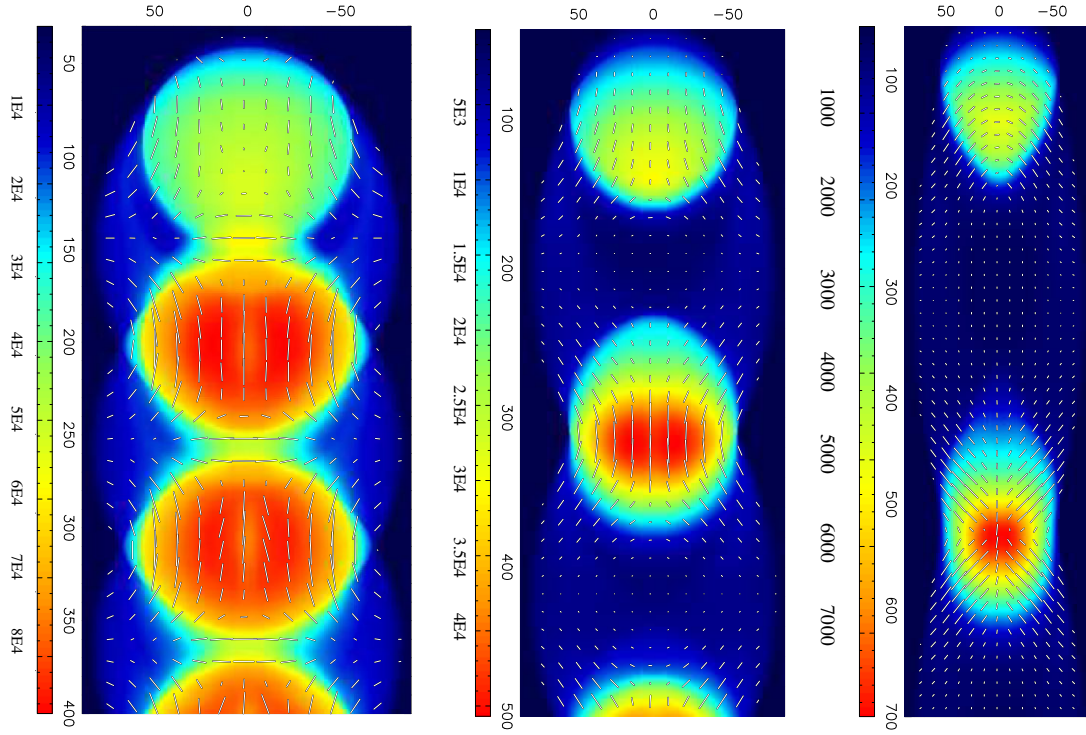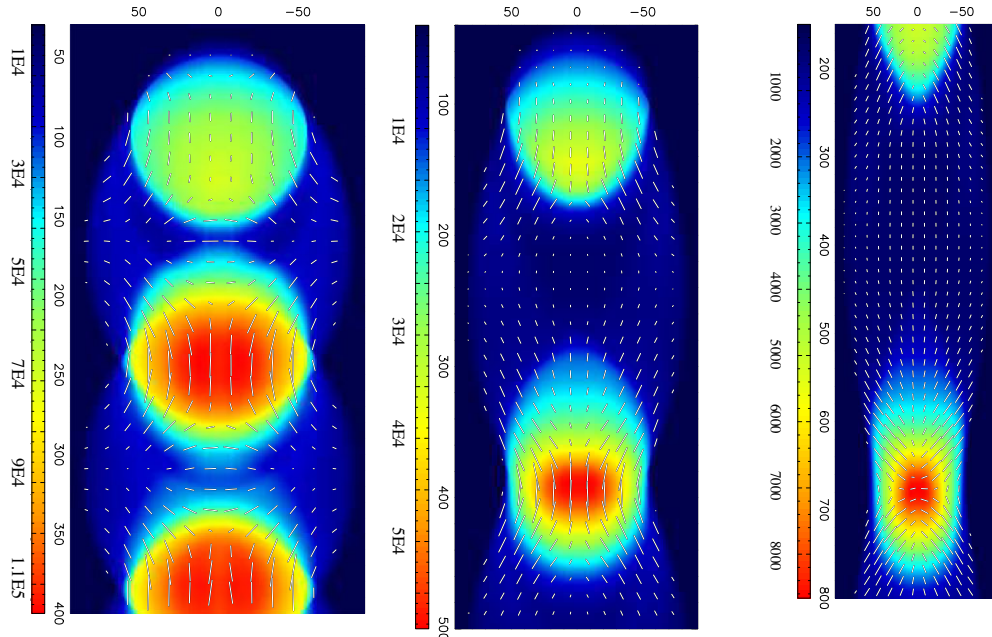
Figure 7. Simulated images of the total intensity (colour scale) for the hot model, overlaid with polarization sticks, are (from left to right) shown for angles $\theta = 5°$, $10°$, and $20°$.

Figure 8. Simulated images of the total intensity (colour scale) for the warm model, overlaid with polarization sticks, are (from left to right) shown for angles $\theta = 5°$, $10°$, and $20°$.

Hence, this is another region where radial stretching of the plasma occurs. These regions, at the edge of the jet, centred near the outline of the incident and reflected shock waves can clearly be seen as areas of high fractional polarization in many of the fractional polarization images shown here.

In the bubbles, the electric field of the polarization indicates directions that, to a first appoximation appear to diverge in a radial

pattern from the pinch points. As noted earlier, the electric field at the centre is parallel to the jet axis at large angles and perpendicular at small angles (at least in the hot and warm simulations). At larger values of θ, the fractional polarization in the bubbles can reach very high values, over 30 per cent in the cold model.

At the pinch points, and for $\theta = 5°$ and $10°$, the polarized electric fields seem to be fairly uniform in direction across the regions of
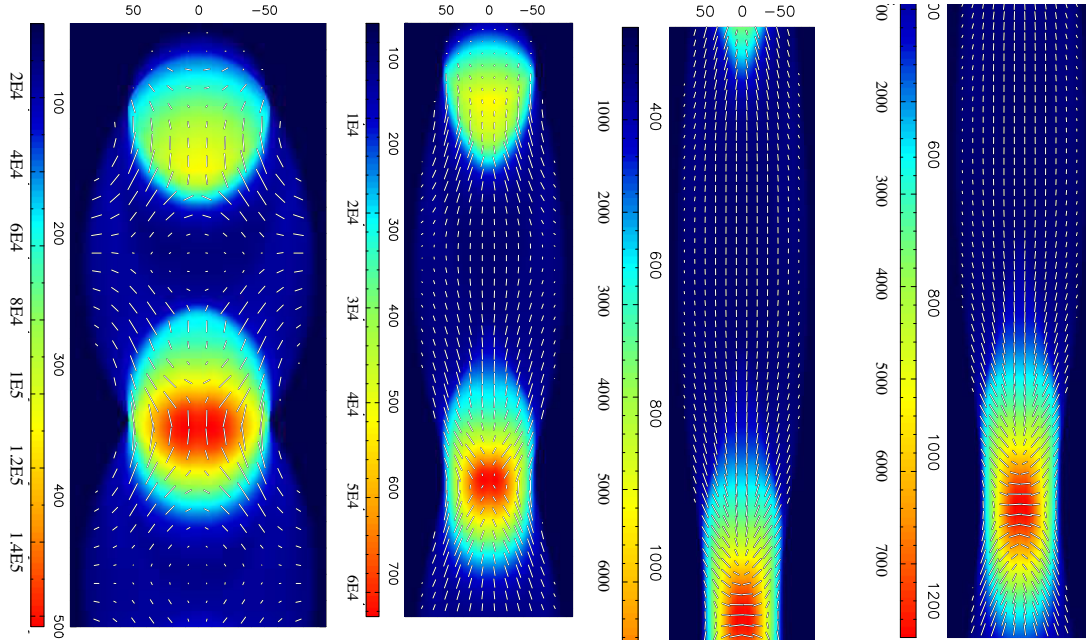
Figure 9. Simulated images of the total intensity (colour scale) for the cold model, overlaid with polarization sticks, are (from left to right) shown for angles 5°, 10°, 20° (near base) and 20° (excluding base).
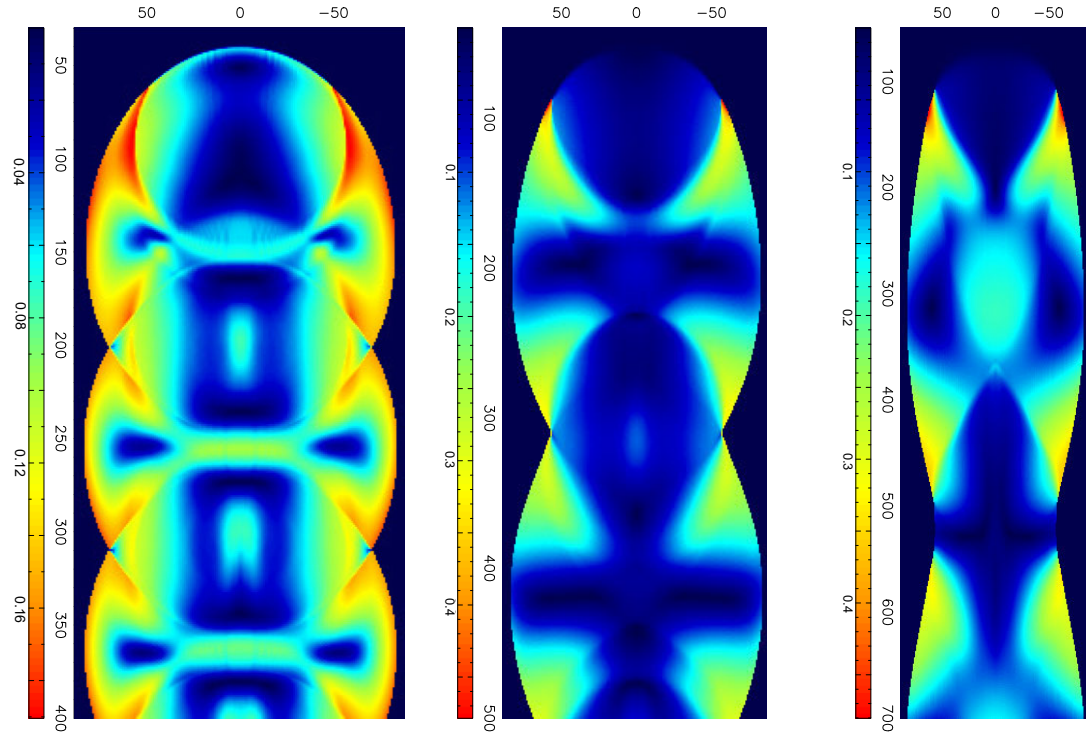
Figure 10. Simulated images of the fractional polarization (colour scale) for the hot model are (from left to right) shown for angles $\theta = 5°$, 10°, and 20°.

bright emission, and parallel to the jet axis. At the larger angle of 20°, the electric field pattern is, to a rough approximation, radial outward from the centre. The fractional polarization is low, typically a few per cent, but reaching 5 per cent in the hot model at $\theta = 10°$.

Lastly here, note that in observation, these distinctive features can be lost easily as a result of poor resolution. Images from the cold simulation (Fig. 9) were convolved with Gaussian beams of increasing size, and by the time the FWHM of the beam reached 10 per cent of the spacing between the jet inlet and the first bright knot, almost all the structure in the distribution of polarization angles had been lost, to be replaced by a nearly uniform pattern, with polarization electric field parallel to the jet axis.
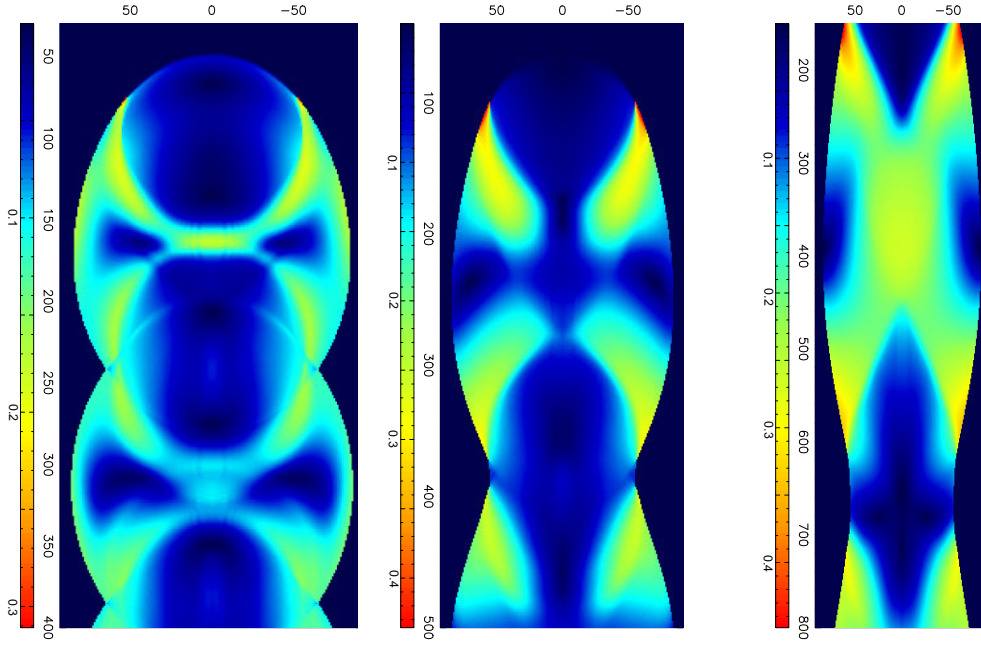
Figure 11. Simulated images of the fractional polarization (colour scale) for the warm model are (from left to right) shown for angles $\theta = 5°,\ 10°$, and $20°$.
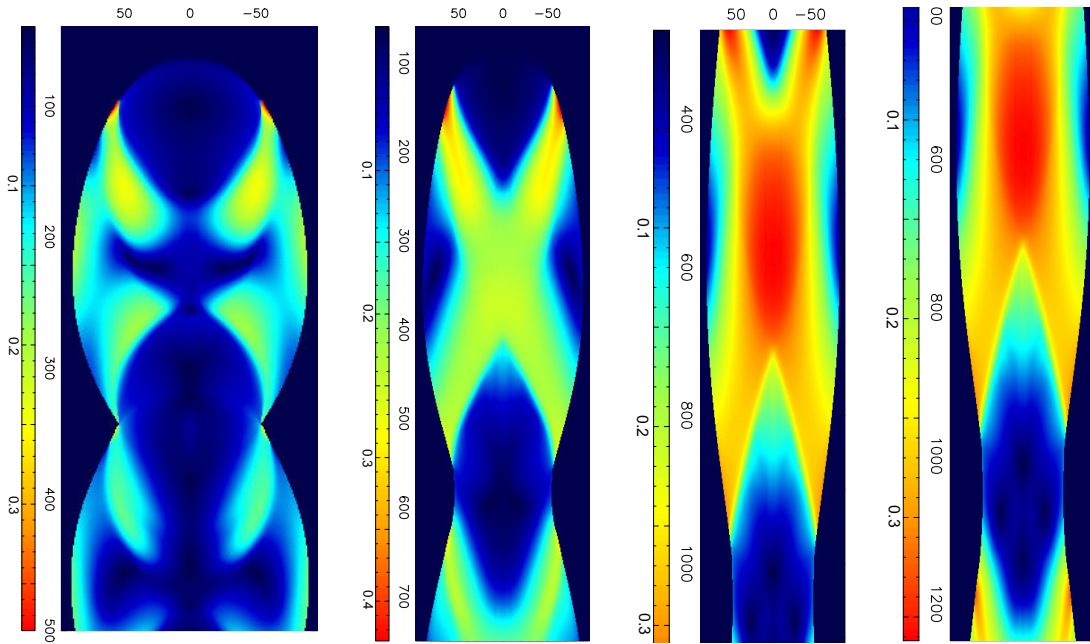

Figure 12. Simulated images of the fractional polarization (colour scale) for the cold model are (from left to right) shown for angles $5°,\ 10°,\ 20°$ (near base) and $20°$ (excluding base).
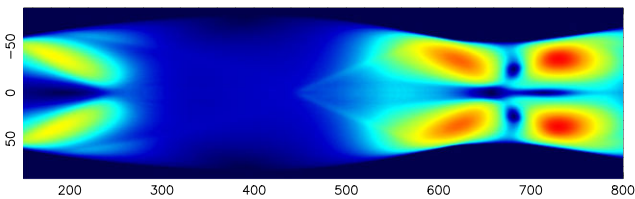

Figure 13. Plot of the polarized intensity for the warm simulation at viewing angle $20°$, showing the slight enhancement of intensity at the position of the reflected shock wave.

11 DISCUSSION

The results presented in this paper depend on the model assumptions made at the outset. First, the magnetic field at injection is disordered on small scales; secondly that it subsequently evolves in a manner determined by magnetic flux freezing and the velocity field of the jet; thirdly, that as a result of being initially over-pressured, the jet undergoes a series of oscillations in diameter, resulting in internal (conical) shock waves. Any correspondence between the results presented here and real images in the literature, could be an indication that the model assumptions are correct.
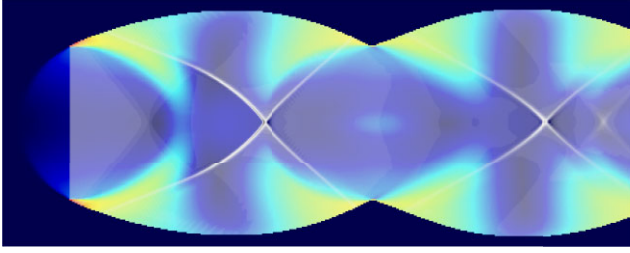
Figure 14. Plot showing the location of the shock wave in relation to the prominent arcs of high fractional polarization in the case of the hot simulation, seen at 10° viewing angle.

Some possible features that might be useful in this respect are discussed below. No attempt is made at detailed comparison with observations, but an example is noted which might warrant further investigation.

It should be remembered that the features modelled in this paper are stationary features in a steady jet, and so comparisons with travelling (superluminal) features should be avoided. Furthermore, no account has been taken of opacity, and the simulated jets, unlike their real counterparts, are contained in a region of uniform density, so there is no systematic expansion along the jet axis. As a result, comparison with observations should be confined to the structure of stationary knots in optically thin parts of radio jets.

Detection of polarization from the weaker interknot regions remains technically challenging and the resolution may not be sufficient to properly separate the knot and interknot polarization. Nevertheless VLBI polarization studies have reported a lower fractional polarization at the bright knots of emission in radio jets, than in the fainter regions in between (e.g. Hutchison, Cawthorne & Gabuzda 2001) in agreement with the simulation results shown here.

The approximately radial patterns of polarization sticks at the bright pinch points seen at large line-of-sight angles, θ, could also be a possible signature of the model. At present the authors are unaware of any observed source features that convincingly show a pattern of this type, though some features in known radio jets might show patterns that could be poorly resolved versions of such a feature. An example is the radio source 0234 + 285 at Epoch 2019 August 15 as seen in the MOJAVE data base (e.g. Lister et al. (2009), and the website described therein). The highly polarized feature near the base of the jet shows electric field of polarization parallel to the axis on axis; just off axis, there is some indication of a radial pattern, but the comparison is complicated by the non-linear structure of the source.

The radio jet associated with 1803 + 784 also shows some similarities with the results presented here. Radio observations were presented by Cawthorne et al. (2013), revealing an unusual radial pattern of polarization angles, two peaks in polarized intensity on axis, and two minima in polarized intensity off axis (see fig. 1 in their paper). This was interpreted in terms of a recollimation shock model in which most of the polarized flux was assumed to arise near the surface of the shock, very different to the situation in the model presented here. At $\theta = 5°$, the cold simulation, Fig. 9 (top panel), shows a pattern of EVPAs qualitatively similar to that found in 1803 + 784; however, the polarization maxima and minima seem to be absent. Nevertheless, the polarization in 1803 + 784 did appear to vary from epoch to epoch, so deviations from the structure at the epoch investigated by Cawthorne et al. (2013) are not conclusive evidence against the model presented here.

The strongly polarized arcs, seen most clearly in the fractional polarization, seem to be the clearest signature of the model presented here. As discussed above, these are caused by radial velocity gradients in the regions where the jets are expanding and contracting, and are associated with, though not coincident with the shock waves. The authors are not aware of any counterparts to these in real observations, but occuring as they do in fainter parts of the jets, this may be a result of limited sensitivity or dynamic range.

12 SUMMARY AND CONCLUSIONS

This paper has presented a method for determining the total intensity and linear polarization distribution of synchrotron radiation using the velocity field of a relativistic steady-state jet simulation. The method traces the development of initially cubic fluid elements into parallelpipeds, and then uses the methods described by Matthews & Scheuer (1990) to determine Stokes parameters from the triad of vectors that span each element. A uniform distribution of fluid elements is ensured by tracing backwards the pathline joining each grid point to a point in the inlet plane, and then tracing forward the corners of the cube centred on that point using the same number of time steps. The method is described for an initially disordered magnetic field, and for some partially ordered magnetic field structures.

Some initial results for the fully disordered field distribution have been presented, based on simulations from the code described by Fuentes et al. (2018). Cases are shown, for initial velocity $0.95c$ (Lorentz factor $\Gamma \simeq 3.2$), and three values of specific internal energy, referred to conveniently as the 'hot', 'warm', and 'cold' simulations.

The results show a series of bright knots separated by fainter 'bubbles', formed as the jet expands, overshooting its equilibrium point, and then contracts again. The variation of the polarization at the centres of the bright knots and bubbles has been described in Section 9. For lines of sight through the bubble's centre, the electric vectors are parallel to the projected jet axis at larger line-of-sight angles, θ, becoming perpendicular at smaller θ; the colder models are generally more highly polarized. For lines of sight through the pinch point, electric vectors are perpendicular to the jet axis at larger θ, becoming parallel at smaller θ; the hotter models are generally more highly polarized.

For each simulation, synthetic images of total intensity with polarization sticks superimposed, and fractional polarization are shown, for line-of-sight angles $\theta = 5°$, $10°$, and $20°$.

The bright knots have low fractional polarization, consistent with the return of the jet plasma to a state near the initial, state, in which its magnetic field was fully disordered. In contrast, the bubbles, though faint, can have quite high levels of fractional polarization, approaching 30 per cent in the cold simulation. The polarization (E field) sticks around the bright knots often adopt a radial pattern, while in the bubbles, they seem to point toward the centres of the nearest knots. Convolution with trial Gaussian beams has shown that these structures can very easily be lost as a result of limited resolution.

The recollimation shocks themselves are not often clearly seen in the images presented here. The reflected (diverging) shock is visible in total intensity (weakly) and more prominently in polarized intensity for the warm simulation at $\theta = 20°$. However, arcs of high fractional polarization resulting from the radial velocity gradients in the vicinity of the shocks are seen in most of the images displayed, and may be a useful diagnostic feature of the model.

The difficulty of imaging faint regions between bright features, together with the limited resolution of radio telescopes makes comparison with observations difficult. As observational techniques

continue to improve, it is to be hoped that a greater level of detail will be detected to allow better comparison between simulations such as these and real radio sources.

DATA AVAILABILITY

The data used in this paper will be shared on reasonable request to the corresponding author.

REFERENCES

Cawthorne T. V., 2006, MNRAS, 367, 851
Cawthorne T. V., Cobb W. K., 1990, ApJ, 350, 536
Cawthorne T. V., Hughes P. A., 2013, ApJ, 771, 60
Cawthorne T. V., Jorstad S. G., Marscher A. P., 2013, ApJ, 772, 14
Falle S. A. E. G., Wilson M. J., 1985, MNRAS, 216, 79
Fuentes A., Gómez J. L., Martí J. M., Perucho M., 2018, ApJ, 860, 121
Fuentes A., Torregrosa I., Martí J. M., Gómez J. L., Perucho M., 2021, A&A, 650, A61
Hughes P. A., Aller H. D., Aller M. F., 1985, ApJ, 298, 301
Hutchison J. M., Cawthorne T. V., Gabuzda D. C., 2001, MNRAS, 321, 525
Jorstad S. G. et al., 2005, AJ, 130, 1418
Jorstad S. G. et al., 2007, AJ, 134, 799
Kaye C., Cawthorne T., Hughes P., 2018, Galaxies, 6, 53
Komissarov S. S., Porth O., Lyutikov M., 2015, Comput. Astrophys. Cosmol., 2, 9
Laing R. A., 1980, MNRAS, 193, 439
Larionov V. M. et al., 2020, MNRAS, 492, 3829
Lister M. L. et al., 2009, AJ, 138, 1874
Lyutikov M., Pariev V. I., Gabuzda D. C., 2005, MNRAS, 360, 869
Marscher A. P., 2014, ApJ, 780, 87
Matthews A. P., Scheuer P. A. G., 1990, MNRAS, 242, 616
Moya-Torregrosa I., Fuentes A., Martí J. M., Gómez J. L., Perucho M., 2021, A&A, 650, A60
Murphy E., Cawthorne T. V., Gabuzda D. C., 2013, MNRAS, 430, 1504
Norman M. L., Winkler K.-H. A., 1985, Supersonic Jets, No. 12 in Los Alamos Science. Los Alamos National Laboratory, Los Alamos, New Mexico, USA
Rybicki G. B., Lightman A. P., 1979, Radiative Processes in Astrophysics. Wiley-Interscience, New York, USA
Warren D. C., Ellison D. C., Bykov A. M., Lee S.-H., 2015, MNRAS, 452, 431

This paper has been typeset from a TEX/LATEX file prepared by the author.